

Article

A Novel Suppression Method for Low-Order Harmonics Causing Resonance of Induction Motor

Pengyun Song ^{1,2}, Yanghui Liu ¹ , Tao Liu ^{1,*}, Huazhang Wang ¹ and Liwei Wang ¹¹ College of Electrical Engineering, Southwest Minzu University, Chengdu 610225, China² Institute of National Productivity Development, Southwest Minzu University, Chengdu 610225, China

* Correspondence: liutao@stu.swun.edu.cn

Abstract: In the motor drive system of electric vehicles, there are some nonlinear factors, such as the deadtime and the conduction voltage drop of switching devices, which will generate low-order harmonics of the stator current and the torque ripple. The frequency of the harmonic may coincide with the natural frequency of the motor, so resonance may occur on the motor drive system. To reduce the noise caused by motor resonance, the characteristics of harmonic distortion caused by the deadtime, and the conduction voltage drop of the switching device, are analyzed firstly. Then, a motor vector control strategy with specific low order is proposed. The sixth-order harmonic resonance controller in d-q axis is introduced into the control loop, and the parameter designing principle of the controller is also presented. Without affecting the control performance of the current loop, the sixth-order harmonic of the stator current near the natural frequency can be significantly suppressed. Finally, the simulation and the experiment are carried out to certify the correctness and effectiveness of the proposed harmonic suppression method.

Keywords: induction motor (IM); harmonic suppression; motor resonance; controller parameter; deadtime; natural frequency



Citation: Song, P.; Liu, Y.; Liu, T.; Wang, H.; Wang, L. A Novel Suppression Method for Low-Order Harmonics Causing Resonance of Induction Motor. *Machines* **2022**, *10*, 1206. <https://doi.org/10.3390/machines10121206>

Academic Editor: Alejandro Gómez Yepes

Received: 3 November 2022

Accepted: 12 December 2022

Published: 13 December 2022

Publisher's Note: MDPI stays neutral with regard to jurisdictional claims in published maps and institutional affiliations.



Copyright: © 2022 by the authors. Licensee MDPI, Basel, Switzerland. This article is an open access article distributed under the terms and conditions of the Creative Commons Attribution (CC BY) license (<https://creativecommons.org/licenses/by/4.0/>).

1. Introduction

The development of electric vehicles is an effective means to solve the problems of energy and environment [1], but serious vibration and noise exist in the motor drive system of the electric vehicle [2]. The output voltage of the inverter is a square wave instead of a sine wave [3], and contains abundant high-order harmonics around the switching frequency and its integer multiples [4]. These higher-order harmonics will lead to serious electromagnetic vibration and noise, and the life and comfort of the electric vehicle are subsequently reduced [5,6]. To reduce the power of the harmonics near the switching frequency, some modulation strategies, such as the random carrier frequency [7] and periodic carrier frequency [8], are proposed. The above methods can disperse the main harmonics spectrum into a wider frequency band, a good suppression effect on the high-frequency noise of the motor caused by the harmonics of stator currents.

Ideally, there is no low-order harmonic in the inverter output voltage [9], but due to nonlinear factors such as the deadtime [10], the conduction voltage drop of switching devices and body diode [11], and the snubber capacitor [12], the lower order harmonics of the stator current will be generated. The natural frequency of the induction motor (IM) for electric vehicles is low, and the operating speed range of IM is wide, so the frequencies of these low-order harmonics may coincide with the natural frequencies of the motor, and the resonance may occur on the motor drive system of the electric vehicle [13]. In reference [14], a reasonable slot fit is selected to weaken the electromagnetic force wave related to electromagnetic vibration, and the vibration peak value of the IM at the natural frequency can be reduced. In reference [15], a Y-type capacitor is introduced at the DC terminal of the inverter; it is particularly effective to reduce the radiation emission of the

vehicle in the above frequency range, and a simplified vehicle common-mode interference model is established. Compared to the above two methods for the structural improvements of the inverter or motor, it is more economical and practical to improve the modulation and control algorithm. Compensation based on pulse time is the most conventional and commonly used low-order harmonic suppression method. According to the polarity of the stator current, the voltage error caused by the deadtime and the conduction voltage drop of switching devices is converted into the duration of PWM pulse, and is subtracted in a switching period [16]. However, the compensation effect of this method is not very obvious. A modulation method without deadtime is proposed in [17]; according to the current polarity, only one switching tube of a phase bridge arm remains in the active state, and the other tube remains OFF state. The freewheeling is completed by the body diode, but the current harmonics caused by the conduction voltage drop of switching devices cannot be suppressed. In reference [18], a feedforward compensation of the average error on the command value is proposed, which can reduce low-order harmonic distortion, but the suppression effect is limited and depends on the sampling accuracy of the current polarity. Reference [19] proposes a scheme for suppressing the 5th and 7th harmonics based on a PI controller, this scheme needs to convert the 5th and 7th harmonic components of the stator current to d-q axis, and then four PI controllers are adopted to obtain the compensation amount of the 5th and 7th harmonics. Although the suppression effect is superior to other methods, the implementation process of this method is a little complicated. In order to suppress the low-order harmonics of the stator current, reference [16] optimizes the current PI controller parameters, but this scheme will reduce the dynamic response speed of the control system. Reference [13] proposes a current spectrum shaping control scheme in the natural frequency range based on a band-pass filter, but the optimal parameters design principle of the band-pass filter is not considered. In reference [20], a frequency adaptive selective harmonic control implemented in Z-plane is proposed for grid-connected inverters, and the fundamental frequency is fixed at 50 Hz. However, the speed range of the motor drive system is wide, the applicability of this method needs further verification. In reference [21], the resonance frequency is adjusted adaptively, however, whether the resonant controller with the same gain and different frequencies will affect the control performance of the current loop needs to be verified. Meanwhile, the calculation expression of the fundamental angle frequency contains IM parameters, rotor flux, stator current in q -axis and speed, so the motor parameters variation and the sampling accuracy will easily lead to the calculation error of the fundamental frequency.

In this paper, the characteristics of harmonic distortion caused by deadtime, and the conduction voltage drop of switching devices, are analyzed first. Then, the vector control scheme is improved, a sixth-order harmonic proportional resonance (PR) controller in d-q axis is introduced in the control loop, and the parameters of the PR controller are optimally tuned in theory. Finally, the simulation and experimental validations of the proposed method are carried out. The research steps are shown in Figure 1.

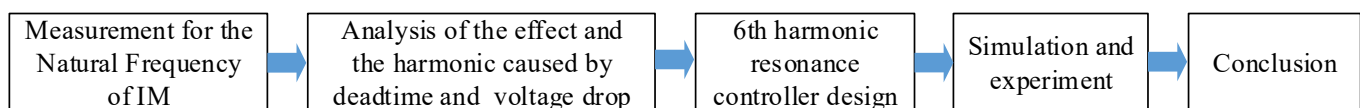


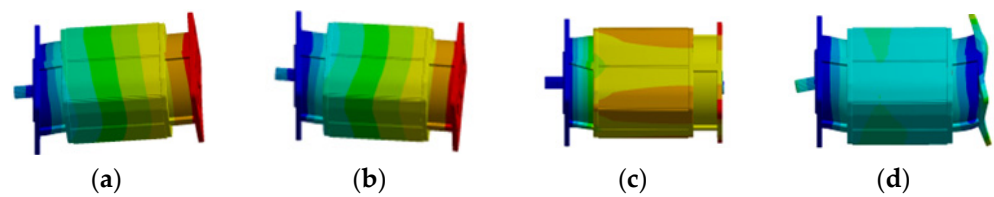
Figure 1. The chart of the research steps for this paper.

2. Simulation and Measurement for the Natural Frequency of IM

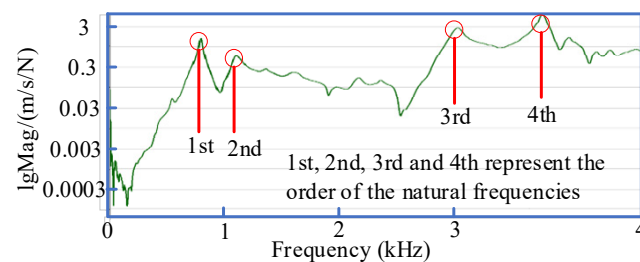
Firstly, the modal analysis of the IM is carried out in ANSYS/Workbench, and the IM parameters are shown in Table 1. One end of the IM is fixed, and a fixed constraint is applied to the other end, the natural frequencies of the IM are obtained by simulation and shown in Figure 2, the 1st to 4th natural frequencies are 850 Hz, 1152 Hz, 3125 Hz and 3893 Hz, respectively.

Table 1. The parameters of the IM.

Parameters	Value	Parameters	Value
Rated voltage	48 V	Rotor outer diameter	109 mm
Rated power	10 kW	Rotor inner diameter	36 mm
Maximum speed	6000 rpm	Rotor slot number	42
Pole pairs	2	Iron core length	180 mm
stator Outer diameter	188 mm	Stator resistance	0.047 Ω
Stator inner diameter	110 mm	Stator leakage inductance	81.5 μ F
stator slot number	36	Rotor resistance	0.028 Ω
Rotor leakage inductance	81.3 μ F	Excitation inductance	2.29 mH

**Figure 2.** Simulation of the IM natural frequency. (a) 1st order modal; (b) 2nd order modal; (c) 3rd order modal; and (d) 4th order modal.

Then, the modal experiment is carried out, the hammering method is adopted to measure the IM natural frequencies, and the vibration intensity of the IM at different frequencies is shown in Figure 3. There are four vibration peak values, the corresponding frequencies are very close to the simulation results.

**Figure 3.** Experimental test of the IM natural frequency.

3. Analysis of Harmonic Characteristics Caused by Nonlinear Factors

Figure 4 shows the topology of the IM drive system fed by the three-phase voltage source inverter (VSI), where u_{dc} is the DC-link voltage, C_{dc} is the DC-link capacitor, S_1 – S_6 is the power switching tube and i_a , i_b , i_c are the three-phase stator currents of the induction motor.

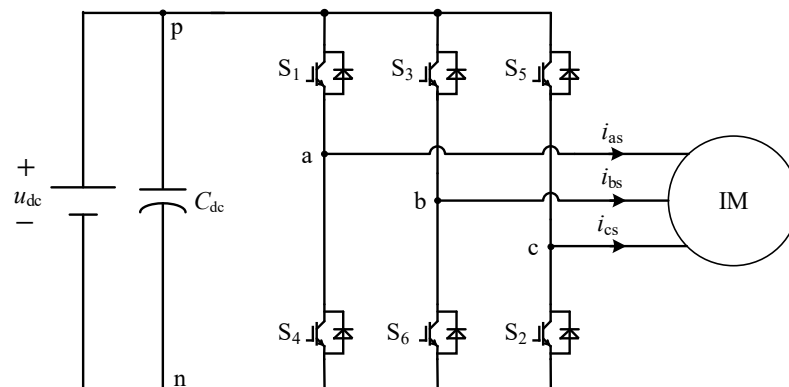
**Figure 4.** The topology of VSI-fed IM drive system.

Figure 5 shows the low-order harmonic distribution of the line-to-line stator voltage u_{ab} and the stator current i_{as} using SVPWM without deadtime and conduction voltage drop of switching devices. Except for the fundamental component, the harmonics of u_{ab} only include the high-order harmonic components around the switching frequency and its integer multiples. So only a few low-order harmonic components exist in the i_{as} .

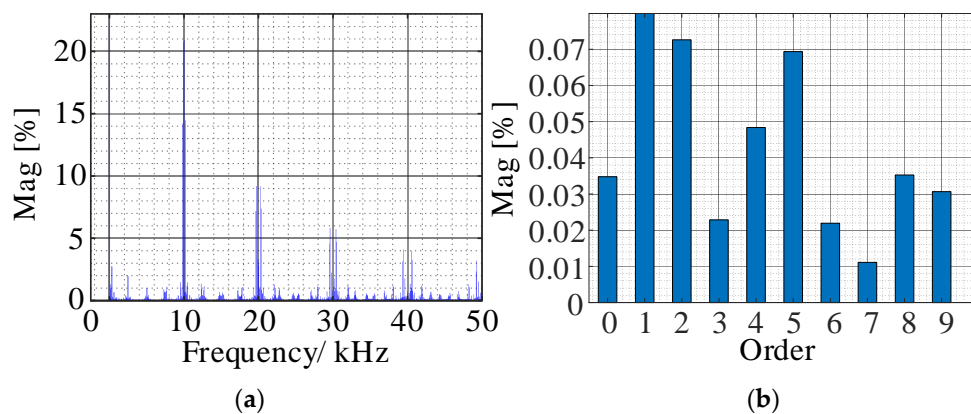


Figure 5. The harmonics distribution without deadtime and conduction voltage drop. (a) u_{ab} ; (b) i_{as} .

If the switching on delay t_{on} and off delay t_{off} are considered, the dead time t_d should be added to prevent the short circuit of the DC battery, the actual switching signals of S_1 and S_4 are noted as p_1 and p_4 , which are shown in Figure 6, an obvious timing error can be seen. At present, the low-order harmonic distribution of the stator current is shown in Figure 7a. Compared to Figure 5b, the 5th and 7th harmonics increase significantly. After setting the conduction voltage drops of the switching tube and body diode, noted as u_{vt} and u_{vd} , respectively, the 5th and 7th harmonics further increase, which is shown in Figure 7b. The output voltage u_{an} of phase a in a switching period T_s is shown in Figure 6, there is a nonlinear error Δu_{an} between u_{an} and the ideal voltage u_{an}^* , and Δu_{an} is affected by the polarity of i_{as} , which is expressed as:

$$\Delta u_{an} = \begin{cases} -[\tau u_{dc} + (d_a - \tau)u_{vt} + (1 - d_a + \tau)u_{vd}] & (i_a > 0) \\ \tau u_{dc} + (1 - d_a - \tau)u_{vt} + (d_a + \tau)u_{vd} & (i_a < 0) \end{cases} \quad (1)$$

where $\tau = (t_d + t_{on} - t_{off})/T_s$, d_a is the duty cycle. These low-order harmonics will increase the torque ripple. If the frequencies of these lower-order harmonics are close to the natural frequencies of the IM, the resonance will occur and the mechanical performance of the IM will deteriorate.

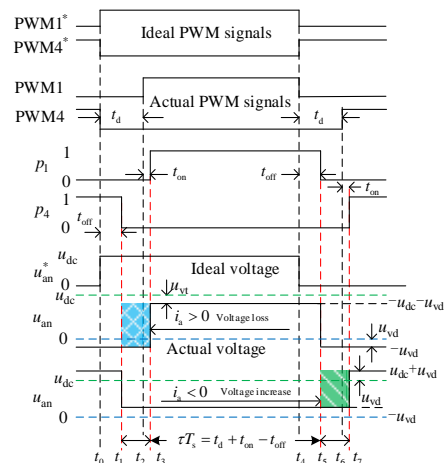


Figure 6. The effect diagram of the deadtime and voltage drops of the switching tube.

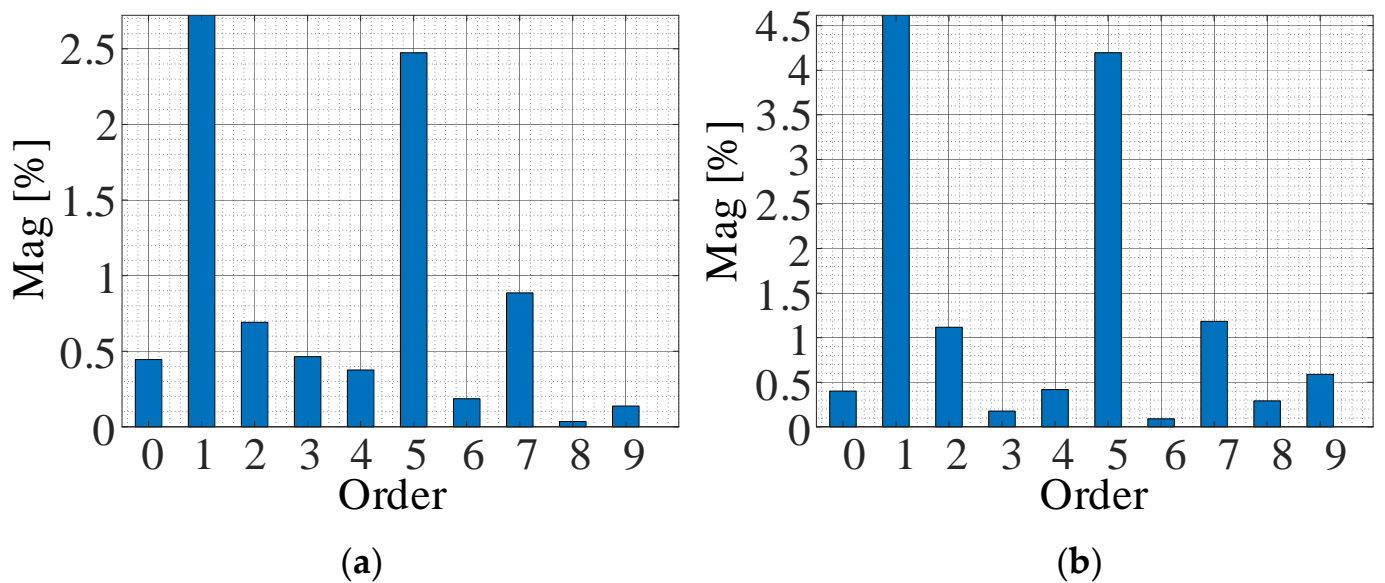


Figure 7. The lower order harmonics distribution of i_{as} . (a) With deadtime; (b) with deadtime and conduction voltage drops.

The sequence of the three-phase 5th harmonic is negative, the expressions of the 5th harmonic component of the three-phase stator current are defined as follows:

$$\begin{cases} i_{a5} = I_5 \sin(5\omega t + \varphi_5) \\ i_{b5} = I_5 \sin(5\omega t + \varphi_5 + 120^\circ) \\ i_{c5} = I_5 \sin(5\omega t + \varphi_5 - 120^\circ) \end{cases} \quad (2)$$

where I_5 and φ_5 are the amplitude and phase of the 5th harmonic component of the stator current, ω is the fundamental angular frequency, respectively. After the coordinate transformation based on the rotor flux orientation, the expressions of the 5th harmonic component of the stator current in d-q axis are obtained as:

$$\begin{cases} i_{d5} = I_5 \cos(6\omega t + \varphi_5) \\ i_{q5} = I_5 \sin(6\omega t + \varphi_5) \end{cases} \quad (3)$$

The sequence of the three-phase 7th harmonic is positive, the expressions of the 7th harmonic component of the three-phase stator current are defined as follows:

$$\begin{cases} i_{a7} = I_7 \sin(5\omega t + \varphi_7) \\ i_{b7} = I_7 \sin(5\omega t + \varphi_7 - 120^\circ) \\ i_{c7} = I_7 \sin(5\omega t + \varphi_7 + 120^\circ) \end{cases} \quad (4)$$

where I_7 and φ_7 are the amplitude and phase of the 7th harmonic component of the stator current, respectively. The expressions of the 7th harmonic component of the stator current in d-q axis are expressed as:

$$\begin{cases} i_{d7} = I_7 \cos(6\omega t + \varphi_7) \\ i_{q7} = I_7 \sin(6\omega t + \varphi_7) \end{cases} \quad (5)$$

Figure 8 shows the low-order harmonics distribution of the stator current in d-q axis, except DC component, the 6th harmonic content is obviously higher than other harmonics in i_d and i_q . Therefore, suppression of the 6th harmonic component of i_d and i_q is equivalent to reducing the 5th and 7th harmonic components of the three-phase stator currents.

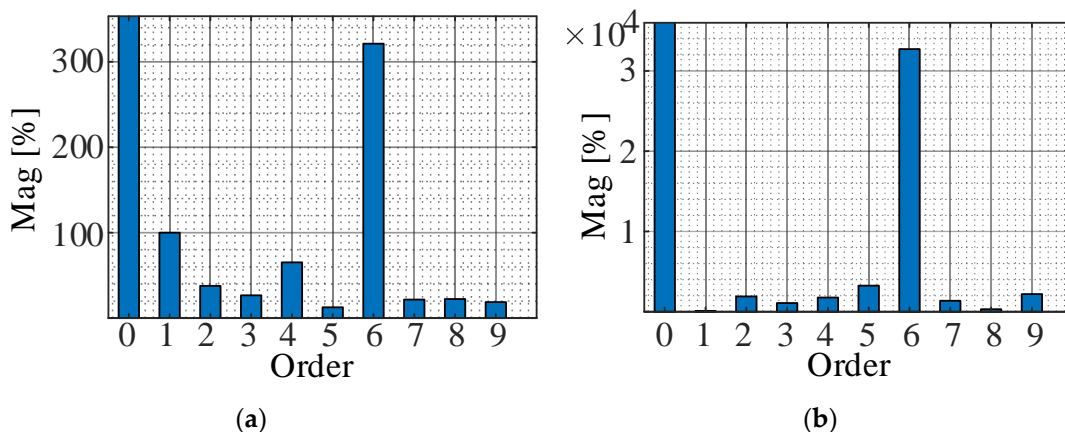


Figure 8. The harmonics distribution of the stator current in d-q axis. (a) i_d ; (b) i_q .

4. Design of Current Loop Controller with 6th Harmonic Suppression

In order to reduce the 6th harmonic content in i_d and i_q , in this paper, a 6th harmonic resonance controller $G_R(s)$ is added to the current loop controller, and the expression of $G_R(s)$ is as follows:

$$G_R(s) = \frac{2k_r \zeta \omega_n s}{s^2 + 2\zeta \omega_n s + \omega_n^2} \tag{6}$$

where ω_n is the resonant frequency, and it is also set as the 6th harmonic angular frequency, ζ is the damping ratio, and k_r is the coefficient of $G_R(s)$. Ignoring the influence of the cross-coupling in d-q axis, the control diagram of the current loop d -axis is shown in Figure 9.

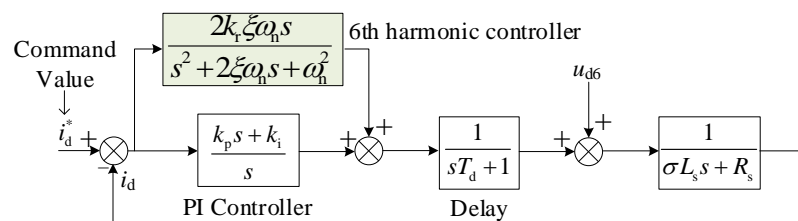


Figure 9. The control diagram of the current loop in d -axis.

Where T_d is the delay time and set as 100 μs in this paper, σ is the leakage coefficient, L_s is the stator equivalent inductance, R_s is the stator resistance of the IM, respectively.

4.1. The Parameters Design of PI Controller

After zero and pole cancellation, the current loop is simplified to a type-I system, the bandwidth of the current inner loop is set as one-tenth of the switching frequency, and the parameters of the PI controller are as follows:

$$\begin{cases} k_p = 2000\pi\sigma L_s \\ k_i = 2000\pi R_s \end{cases} \tag{7}$$

The open loop transfer function $G_{i_ol}(s)$ of the current loop without $G_R(s)$ can be expressed as:

$$G_{i_ol}(s) = \frac{2000\pi}{s(T_d s + 1)} \tag{8}$$

The close loop transfer function $G_{i_cl}(s)$ of the current loop can be derived as:

$$G_{i_cl}(s) = \frac{G_{i_ol}(s)}{1 + G_{i_ol}(s)} = \frac{2000\pi}{T_d s^2 + s + 2000\pi} \tag{9}$$

The bode plot of $G_{i_{cl}}(s)$ is shown in Figure 10a, the bandwidth is 1 kHz, which is one-tenth of the switching frequency. The 6th harmonic distortion caused by the deadtime and conduction voltage drop in d-q axis is regarded as a disturbance u_{d6} , the expression of the transfer function $G_{u_i}(s)$ from u_{d6} to i_d can be derived as:

$$G_{u_i}(s) = \frac{s(T_d s + 1)}{\sigma L_s T_d s^3 + (R_s T_d + \sigma L_s) s^2 + R_s s + 2000\pi} \quad (10)$$

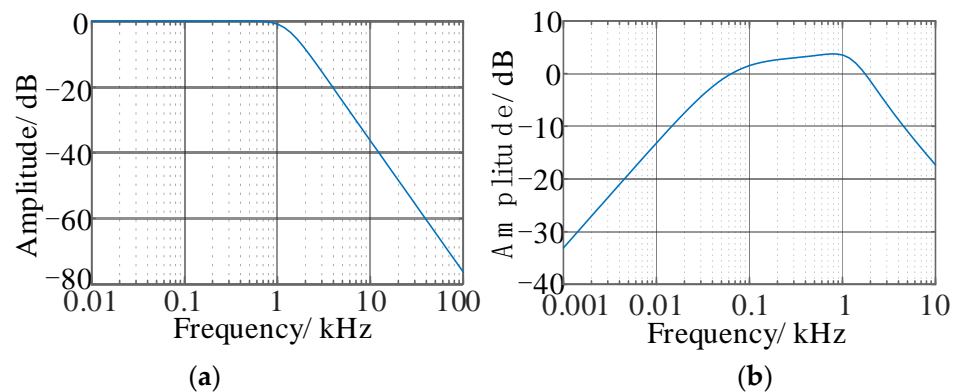


Figure 10. The bode plots without resonance controller. (a) $G_{i_{cl}}(s)$; (b) $G_{u_i}(s)$.

The bode plot of $G_{u_i}(s)$ is shown in Figure 10b, it can be seen that the amplitude of $G_{u_i}(s)$ in the range of 70 Hz to 1.8 kHz is above 0 dB line, so the PI controller is not able to suppress the low order harmonic distortion of the stator current caused by the disturbance voltage in the range of 70 Hz to 1.8 kHz.

4.2. The Parameters Design of Resonance Controller

Next, the influence of different k_r on control performance will be discussed. When the fundamental frequency of the stator current is 167 Hz, the 5th and 7th harmonic frequencies are 835 Hz and 1169 Hz, respectively, which coincides with the 1st and 2nd natural frequencies of the IM. So ω_n in $G_R(s)$ is set to 1002π rad/s, which is equal to six times the fundamental angular frequency, and ζ is set as 0.5. When $G_R(s)$ is introduced, the bode plot of $G_{i_{ol}}(s)$ under different k_r is shown in Figure 11. It can be seen that the addition of $G_R(s)$ has no impact on the low-frequency characteristic of $G_{i_{ol}}(s)$, but with the increase of k_r , the amplitude around 1000 Hz increases significantly, the cut-off frequency also increases as the k_r , but the phase margin of $G_{i_{ol}}(s)$ decreases, which may lead to the system instability.

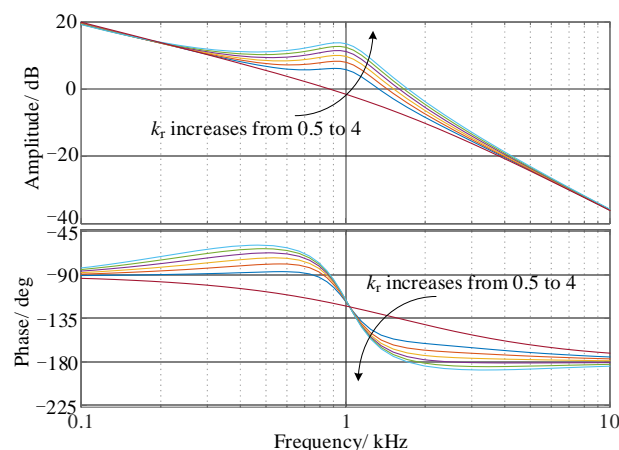


Figure 11. The bode plot of $G_{i_{ol}}(s)$ with resonance controller under different k_r .

To further analyze the influence of k_r on stability, when k_r increases from 1 to 4, the pole distribution diagram of $G_{i_cl}(s)$ is shown in Figure 12. As k_r increases, a pair of conjugate poles move to the right. When $k_r > 3.5$, $G_{i_cl}(s)$ appears on the right half-plane pole, which leads to system instability.

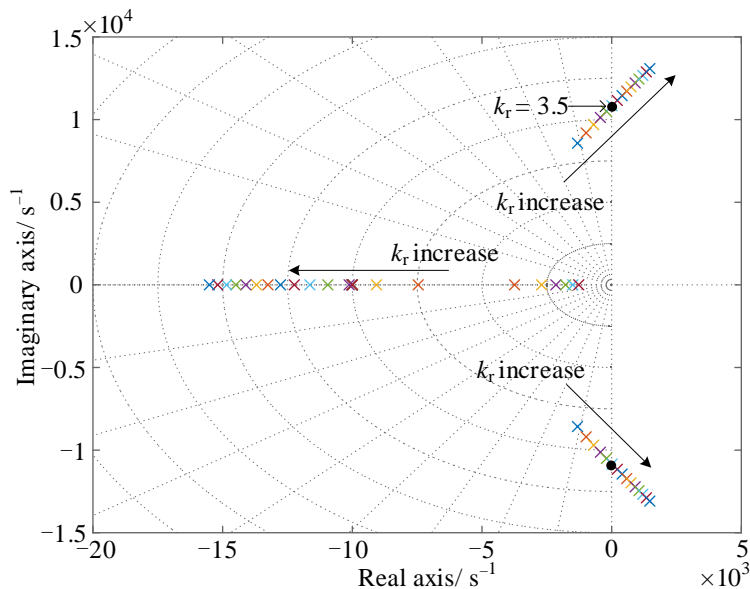


Figure 12. The pole distribution diagram of $G_{i_cl}(s)$ under different k_r .

In order to theoretically prove the suppression effect of $G_R(s)$ on the 6th harmonic component in i_d , when k_r increases from 1 to 3, the bode plot of $G_{u_i}(s)$ is shown in Figure 13. Due to the addition of $G_R(s)$, the amplitude around 1000 Hz is below 0 dB line. And with the increase of k_r , the suppression effect on the 6th harmonic component in i_d is more significant, and the band of the voltage harmonic frequency that can be suppressed by the $G_R(s)$ will also expand. Although another peak appears, the amplitude of the harmonic components of the inverter output voltage in d-q axis is very few, so it will not cause additional harmonic distortion. However, to prevent increasing the eleventh and thirteenth harmonics of stator current, the cut-off frequency of $G_{u_i}(s)$ should be less than the twelfth harmonic frequency.

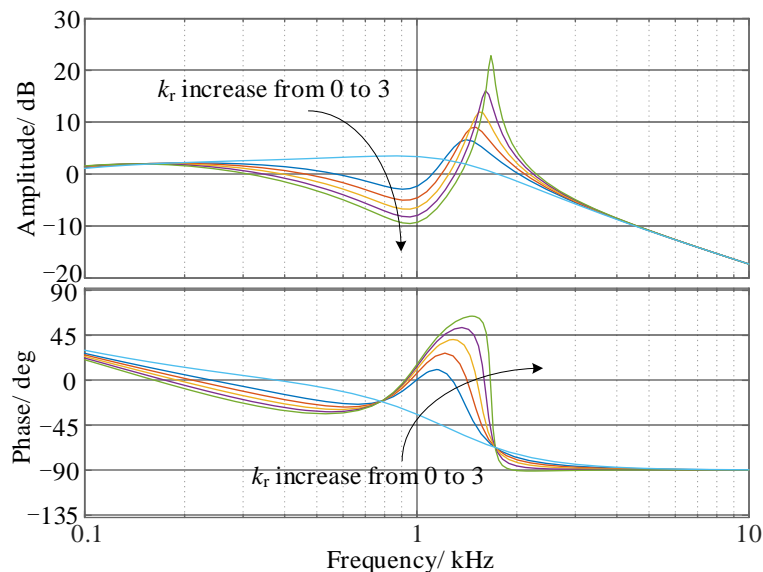


Figure 13. The bode plot of $G_{u_i}(s)$ with resonance controller under different k_r .

4.3. Analysis of the Resonance Controller under Frequency Variation

According to the above analysis presented in Section 4.2, the suppression effect can be improved with the increase of k_r , however, the stability of the current loop is reduced, so k_r is set to 2.5 in this paper, and the transfer function of $G_R(s)$ is shown as:

$$G_R(s) = \frac{2505\pi s}{s^2 + 1002\pi s + (1002\pi)^2} \tag{11}$$

The bode plot of $G_{u_i}(s)$ is shown in Figure 14. It can be seen that the resonance controller can suppress the stator voltage whose 6th harmonic frequency is between 0.35 kHz and 1.32 kHz. However, if the 6th harmonic frequency is between 0.065 kHz and 0.35 kHz, the corresponding fundamental frequency is between 10.8 Hz and 58.3 Hz, the resonance controller under $k_r = 2.5$ and $\omega_n = 1002\pi$ rad/s is not able to suppress the harmonic distortion caused by the deadtime and the voltage drops of switching devices and diode.

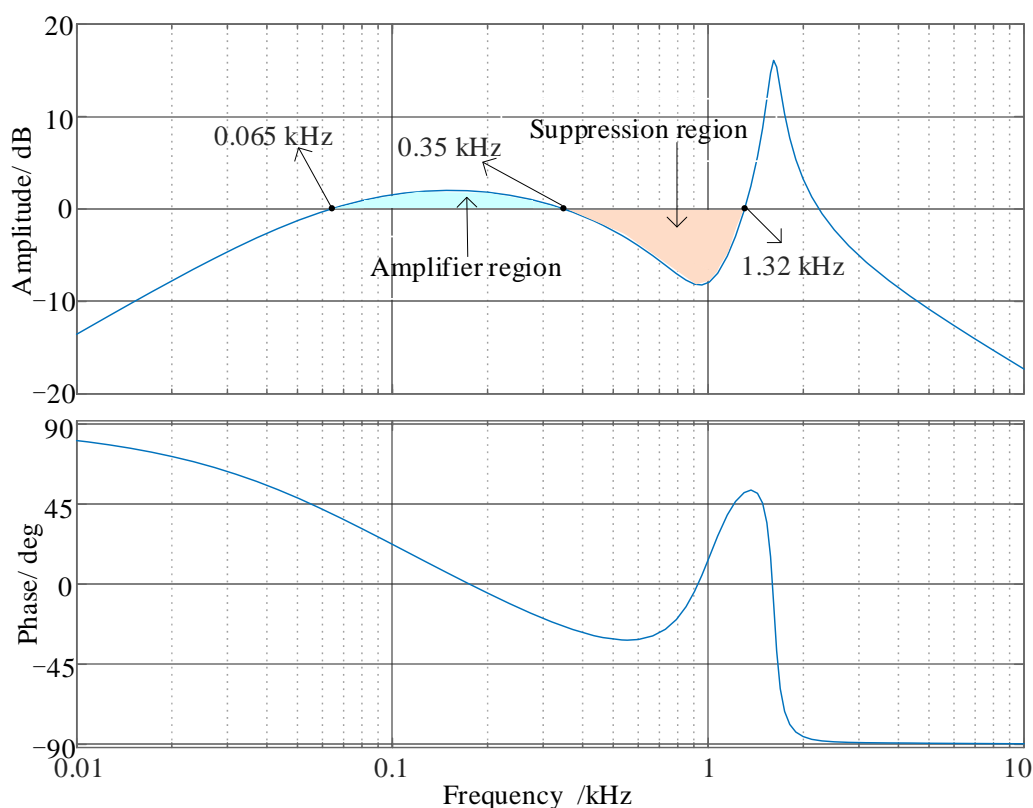
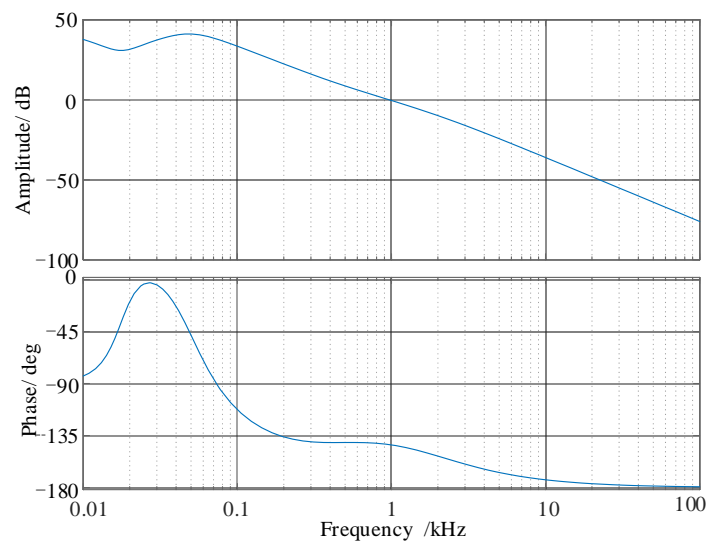


Figure 14. The bode plot of $G_{u_i}(s)$ with resonance controller under $k_r = 2.5$ and $\omega_n = 1002\pi$ rad/s.

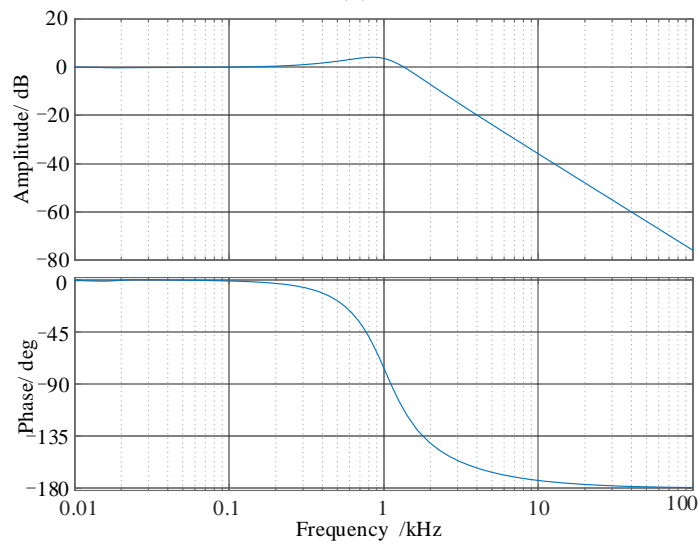
In the case where the fundamental frequency is less than 60 Hz. Another resonance controller is designed and adopted. In consideration of the stability and the harmonic suppression effect, according to the bode plot and the pole distribution diagram, the transfer function $G_R(s)$ is rewritten as:

$$G_R(s) = \frac{600\pi s}{s^2 + 100\pi s + 10000\pi^2} \tag{12}$$

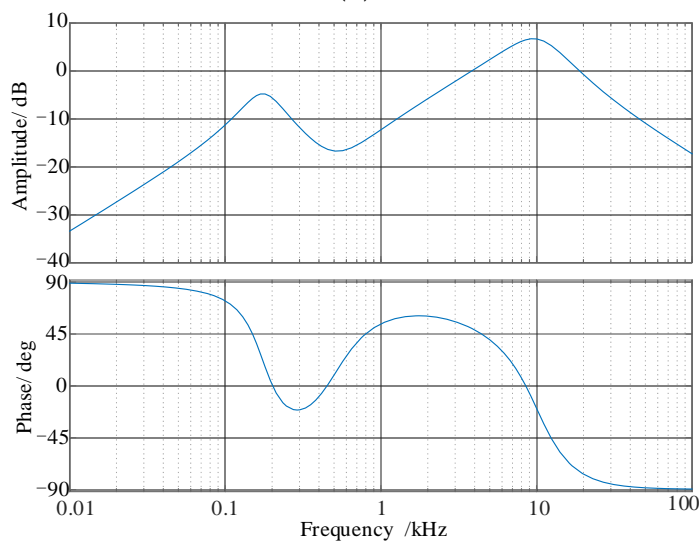
At this time, the bode plots of $G_{i_{ol}}(s)$, $G_{i_{cl}}(s)$, and $G_{u_i}(s)$ are shown in Figure 15. It can be seen that the cut-off frequency of $G_{i_{ol}}(s)$ is 1 kHz, the phase margin of $G_{i_{ol}}(s)$ is 45° , and $G_{i_{cl}}(s)$ has a good DC following characteristics. Meanwhile, the resonance controller shown in Formula (10) can effectively suppress the disturbance from the stator voltage whose 6th harmonic frequency is less than 0.38 kHz.



(a)



(b)



(c)

Figure 15. The bode plots the fundamental frequency is less than 60 Hz. (a) $G_{i_{ol}}(s)$; (b) $G_{i_{cl}}(s)$; and (c) $G_{u_i}(s)$.

Since the two resonant controllers shown in Formulas (11) and (12) are applicable to different frequency ranges, the resonant controller needs to be selected according to the fundamental frequency. The fundamental angle frequency ω_s can be calculated by the follows:

$$\omega_s = n\omega_r + \frac{L_m R_r i_q}{L_r \psi_r} \tag{13}$$

where R_r is the rotor resistance, ψ_r is the rotor flux, ω_r is the speed, and n is the number of pole pairs. L_m and L_r are the mutual inductance and rotor inductance, respectively. The fundamental frequency $f_s = \omega_s / (2\pi)$, if $f_s > 60$ Hz, the $G_R(s)$ shown as (11) is adopted, otherwise, the $G_{R'}(s)$ shown as (12) is adopted.

5. Simulation Results

In order to verify the suppression effect of the proposed method in this paper on the low-order harmonics in the stator current, the simulation model is established in the environment of Matlab/Simulink. The IM parameters are the same as in Table 1, other parameters are set in Table 2.

Table 2. Simulation parameters.

Parameters	Value	Parameters	Value
Switching cycle	10 kHz	Simulation step size	0.5 μ s
Sampling cycle	10 kHz	Voltage drop of the switching devices	0.5 V
Deadtime	2 μ s	Voltage drop of the diode	0.7 V

In order to unify with the digital control in the experiment, the controller composed PI and resonance is implemented by a Matlab function module in the environment of Matlab/Simulink, and the sampling time is set as 100 μ s. According to the difference equation, the discrete control algorithm is written in the Matlab function module, which is shown as:

$$u_d^*(k) = (3 - 2\xi\omega_n T_s)u_d^*(k-1) - (1 - 2\xi\omega_n T_s + \omega_n^2 T_s^2)u_d^*(k-2) + (k_i T_s + k_p)e(k) + 2k_r \xi \omega_n T_s e(k-1) - 2k_r \xi \omega_n e(k-2) \tag{14}$$

where e is the current error. The fundamental frequency and the load are set as 167 Hz and N·m, respectively. Three different simulations are carried out under no compensation, pulse time compensation, and the 6th harmonic controller in d-q axis proposed in this paper, respectively. The simulation results under different conditions are shown in Figures 16–18, respectively. The THD, 5th harmonic, and 7th harmonic of the stator current, and the torque ripple, are summarized in Table 3; it can be seen that the low order harmonics suppression effect of the 6th harmonic controller in d-q axis is optimal.

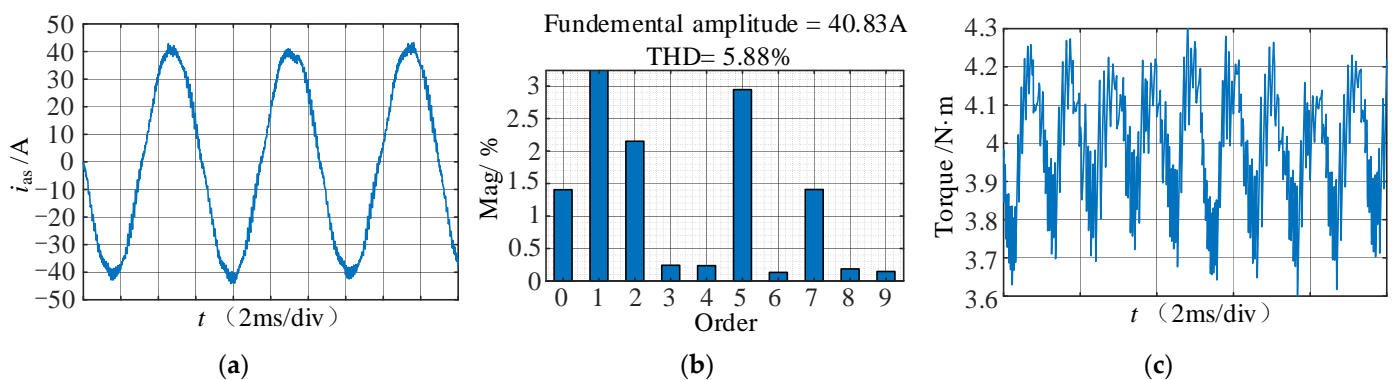


Figure 16. Simulation results under no compensation. (a) i_{as} ; (b) FFT; and (c) output torque.

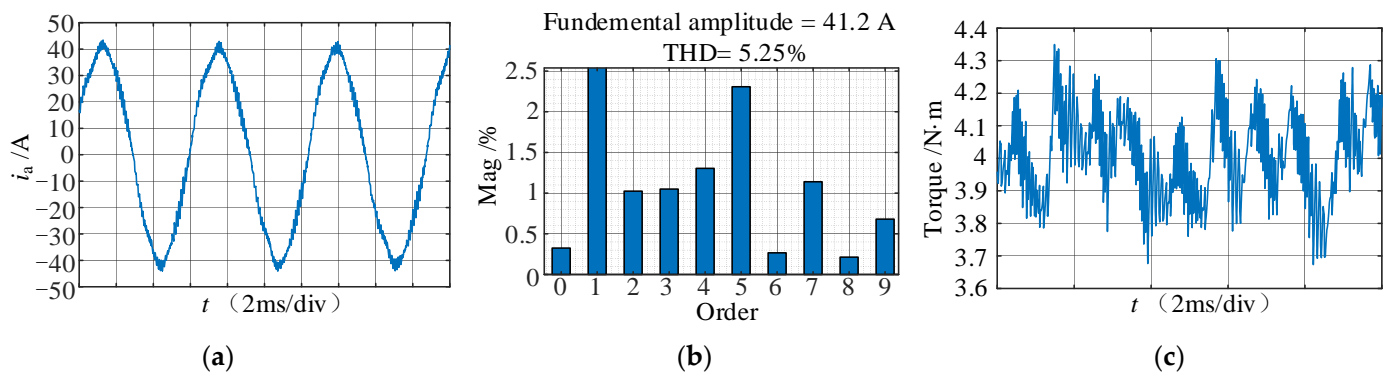


Figure 17. Simulation results under pulse time compensation. (a) i_{as} ; (b) FFT; and (c) output torque.

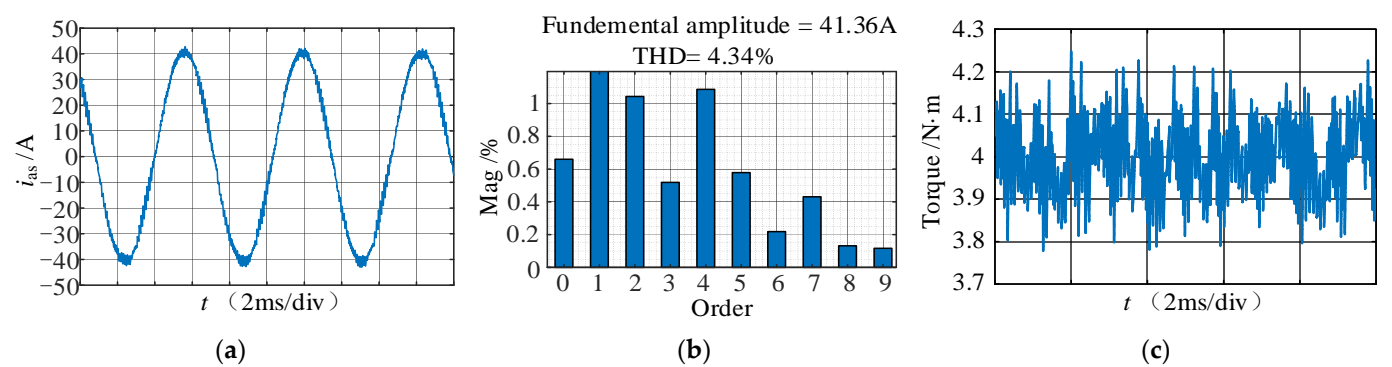


Figure 18. Simulation results under 6th harmonic controller. (a) i_{as} ; (b) FFT; and (c) output torque.

Table 3. Comparison of the simulation results.

Compensation Method	THD	5th Harmonic	7th Harmonic	Torque Ripple (N·m)
No compensation	5.88%	2.9%	1.4%	3.6 to 4.3
Pulse time compensation	5.33%	2.3%	1.2%	3.7 to 4.3
6th harmonic controller	4.34%	0.58%	0.43%	3.8 to 4.2

To certify the effectiveness of the resonant controller shown in Formula (12) at low frequency, the fundamental frequency is set as 30 Hz, two simulations are carried out by the controller (11) and (12), respectively. The low-order harmonics distribution of the stator current is shown in Figure 19. It is obvious that the resonant controller of (11) cannot suppress the 5th and 7th harmonic components of the stator current. As opposed to this, the 5th and 7th harmonic components are significantly reduced when the resonant controller of (12) is adopted.

Next, the impact on the dynamic performance of the system from the resonant controller is verified. Firstly, the load torque is set to 4 N·m constantly, and the command value of speed changes from 3000 rpm to 4500 rpm, the dynamic simulation results with and without the resonant controller are shown in Figure 20. Then, the command value of speed is set to 4000 rpm, the load torque increases from 2 N·m to 4 N·m, and the dynamic simulation results with and without the resonant controller are shown in Figure 21. After the resonant controller is introduced, only a slight difference occurs in the dynamic waveforms of speed and torque, so the resonant controller has no impact on the dynamic performance.

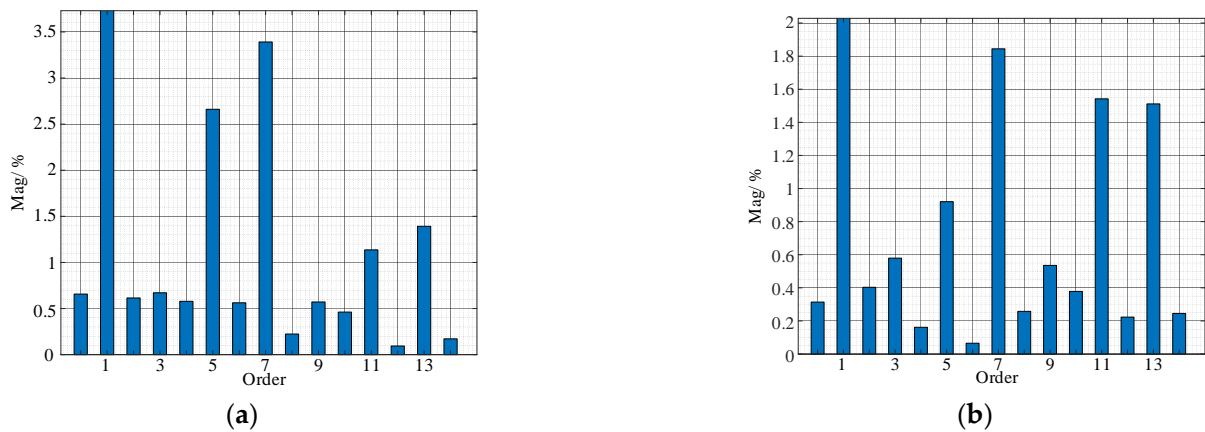


Figure 19. The FFT analysis results of the stator current under different resonant controllers. (a) $G_R(s)$ of (11); (b) $G_R(s)$ of (12).

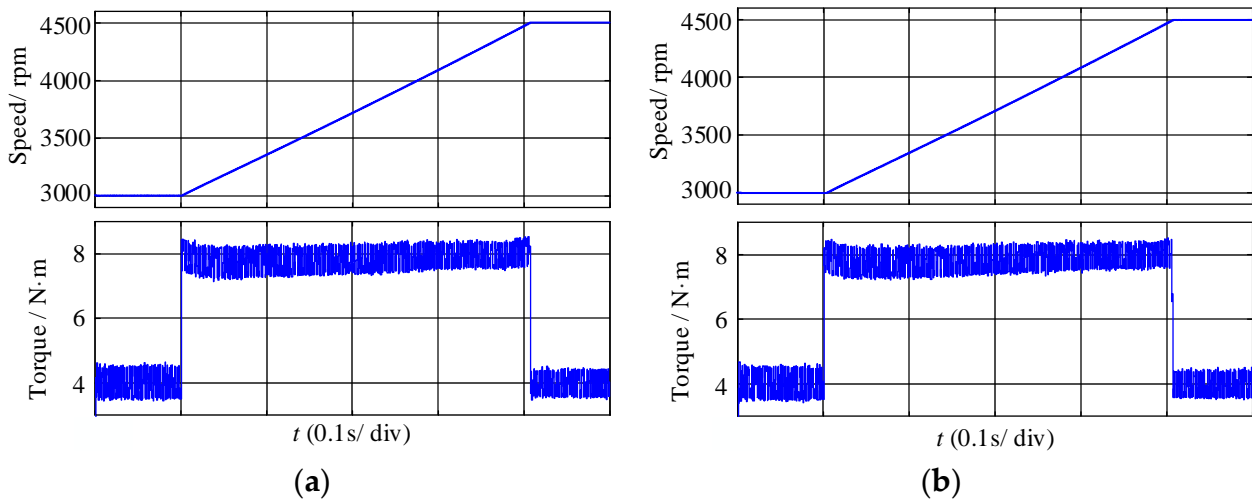


Figure 20. The dynamic simulation waveforms when the speed changes from 3000 rpm to 4500 rpm. (a) Without resonant controller; (b) with resonant controller.

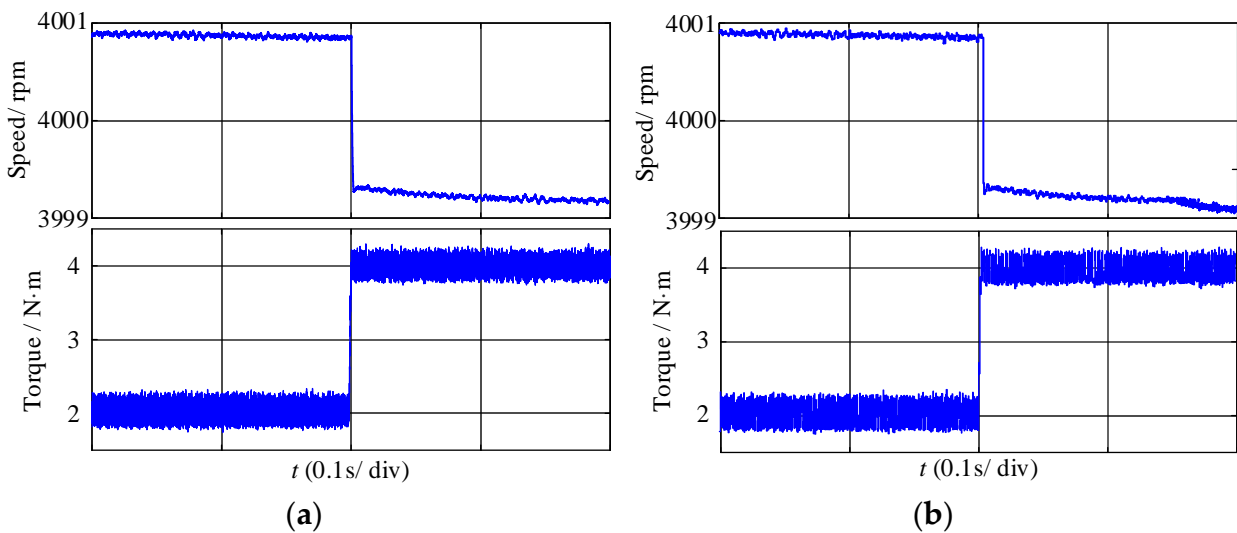


Figure 21. The dynamic simulation waveforms when the load changes from 2 N·m to 4 N·m. (a) Without resonant controller; (b) with resonant controller.

6. Experimental Results

The experimental prototype, shown in Figure 22, is established to verify the suppression effect of the proposed method on the low-order harmonics in the stator current. TMS320F28069 is used to execute the control algorithm, and three non-contact sensors MLX91205 is used to sample the stator current. The inverter bridge is composed by the MOSFET, the type is IPB042N10N, the DC-link voltage is 72 V, and is supplied by the battery pack. The parameters of the IM are the same as in Table 1, and the experimental parameters and operation are the same as in Table 2. The experimental results under no compensation, pulse time compensation, and the 6th harmonic controller in d-q axis are shown in Figures 23–25, respectively. Under the influence of deadtime and conduction voltage drop, without compensation, the stator current has serious harmonic distortion, the 5th harmonic content is 3.2%, the 7th harmonic content is 2.3%, and there is a little DC component. After the pulse time compensation, the content of the 5th and 7th harmonics and THD are slightly reduced, and the power spectral density at the natural frequency drops below -10 dB/Hz. By adopting the 6th harmonic controller in d-q axis proposed in this paper, the 5th harmonic content is only 1%, the 7th harmonic content 0.6%, and the THD decreases to 4.62%. At the same time, the DC component of the current is eliminated, and the power spectral density at all frequencies is less than -20 dB/Hz. The experimental results are consistent with the simulation results, which show that the proposed resonant controller in d-q axis can reduce the low-order harmonics of the stator current.

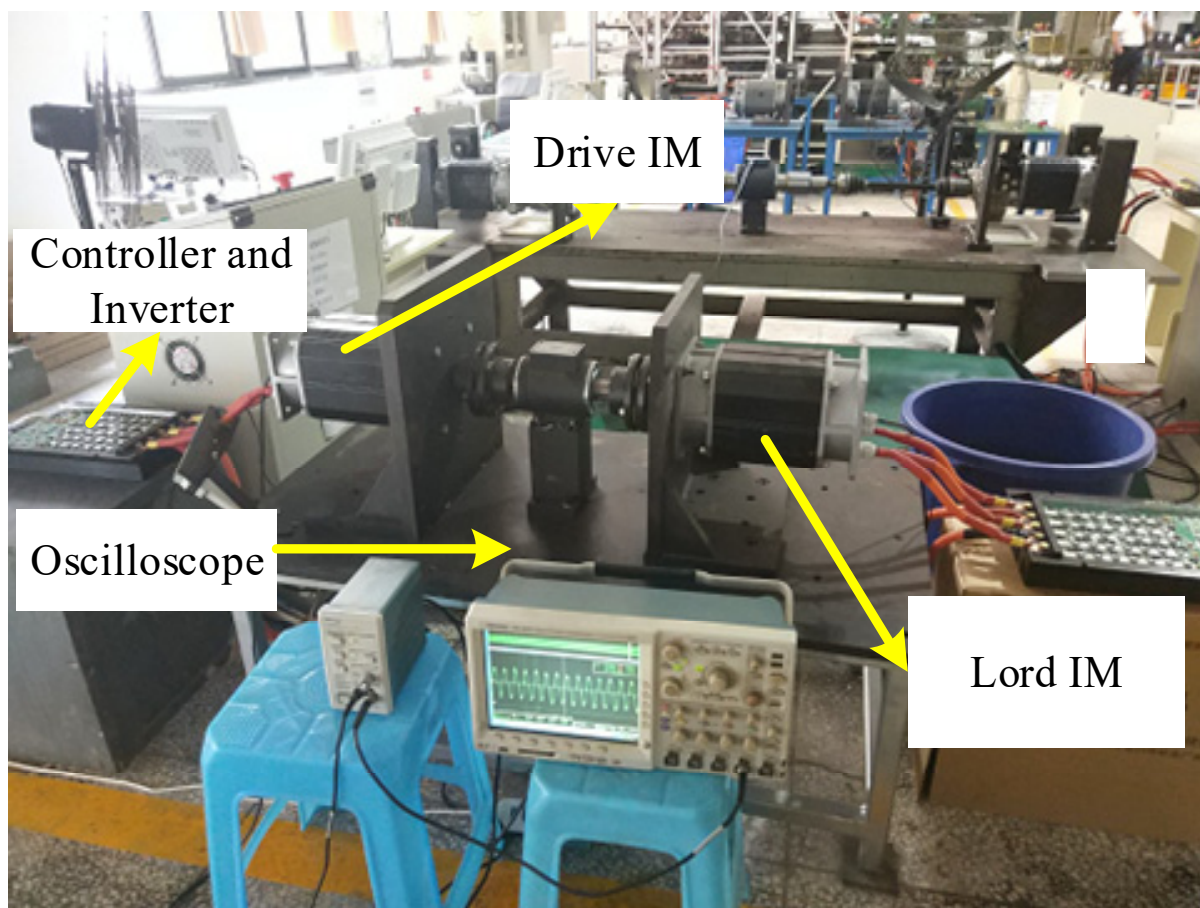


Figure 22. Experimental prototype.

To verify the effectiveness of the control algorithm in reducing vibration, a vibration measurement instrument is used to measure the vibration of the IM, and the measurement experiment platform is shown in Figure 26.

Figure 27 shows the power spectral density of the vibration within 1.8 kHz under no compensation, there are two peaks of vibration at the 1st and 2nd natural frequencies. Figure 28 shows the power spectral density of the vibration within 1.8 kHz under the 6th harmonic controller in d-q axis, the vibrations are significantly suppressed. The whole experimental results further prove that the 6th harmonic controller with its parameter design method in d-q axis has a good suppression effect on the 5th and 7th harmonics distortion of the stator current, which can not only reduce the torque ripple, but also weaken the vibration of the IM.

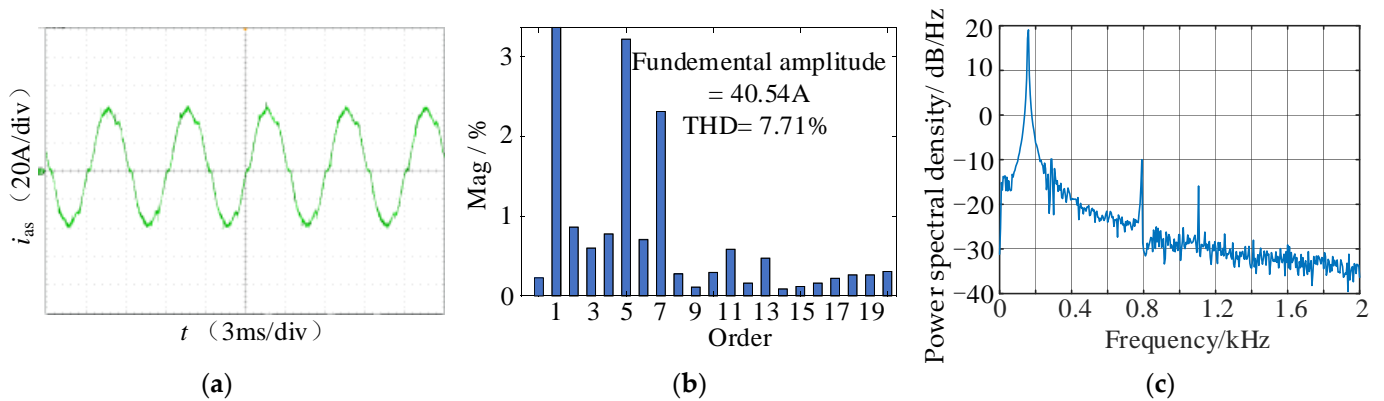


Figure 23. Experimental results under no compensation. (a) i_{as} ; (b) FFT; and (c) power spectral density.

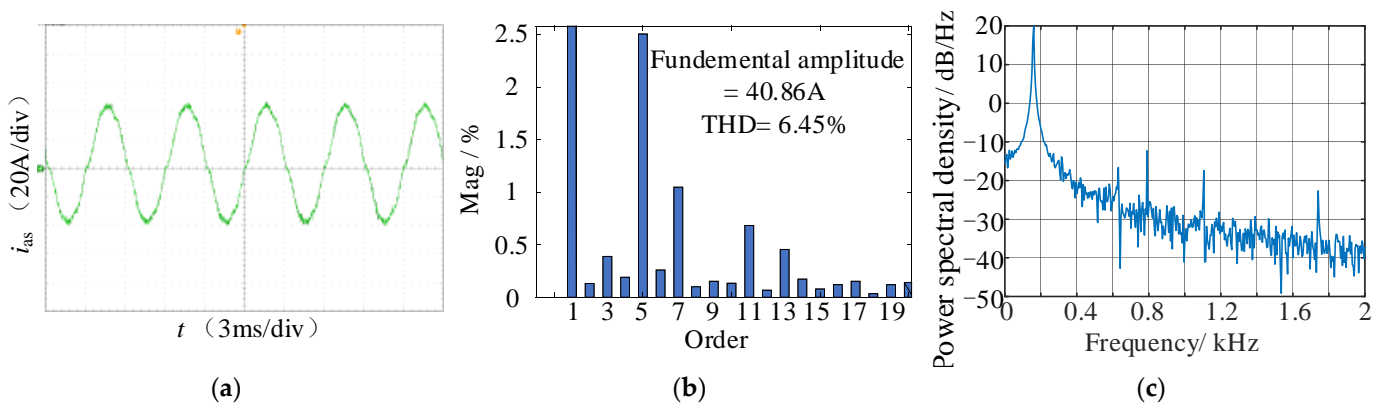


Figure 24. Experimental results under pulse time compensation. (a) i_{as} ; (b) FFT; (c) Power spectral density.

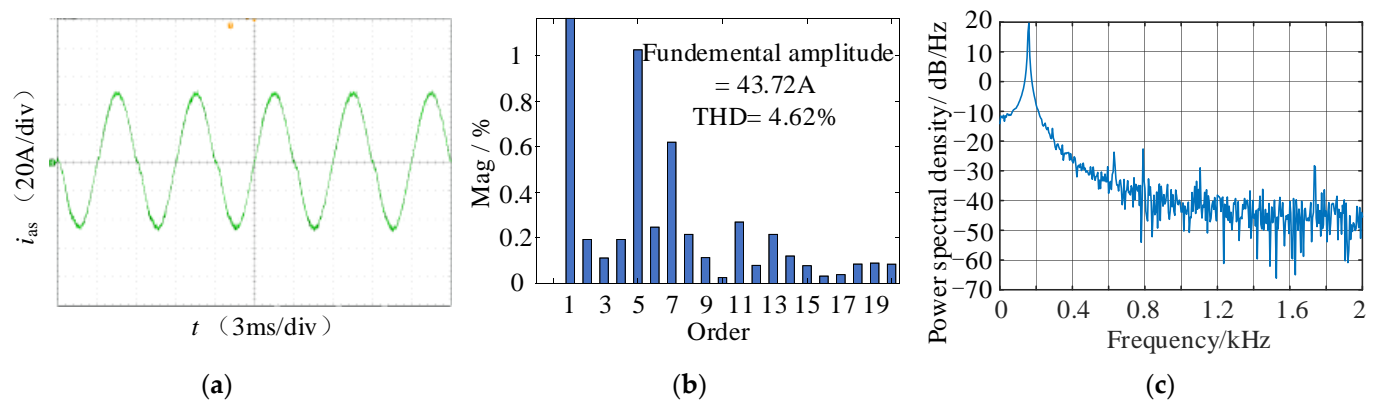


Figure 25. Experimental results under 6th harmonic controller. (a) i_{as} ; (b) FFT; and (c) power spectral density.

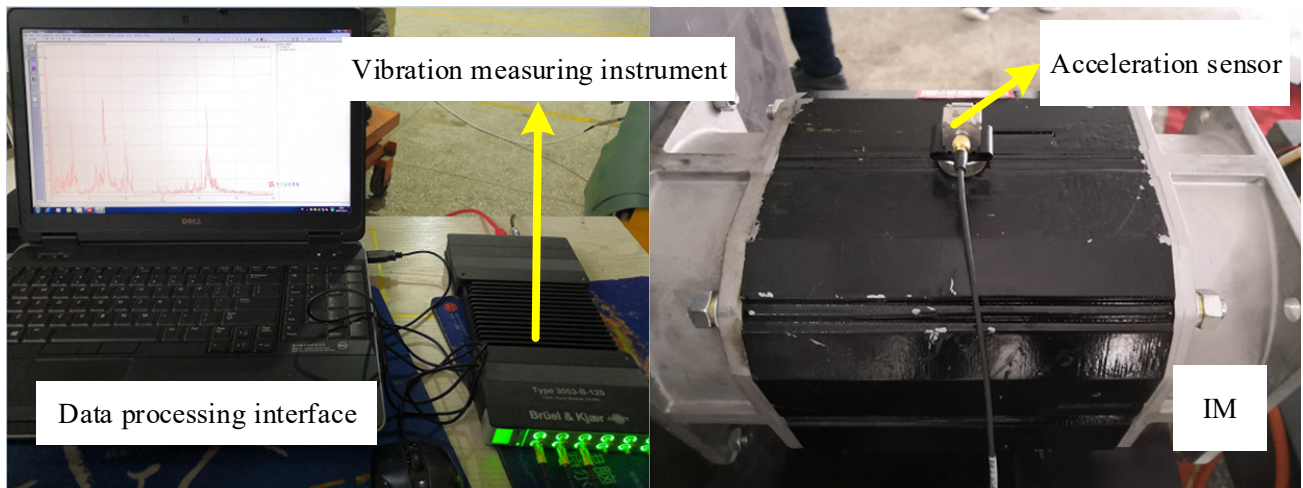


Figure 26. The vibration measurement platform.

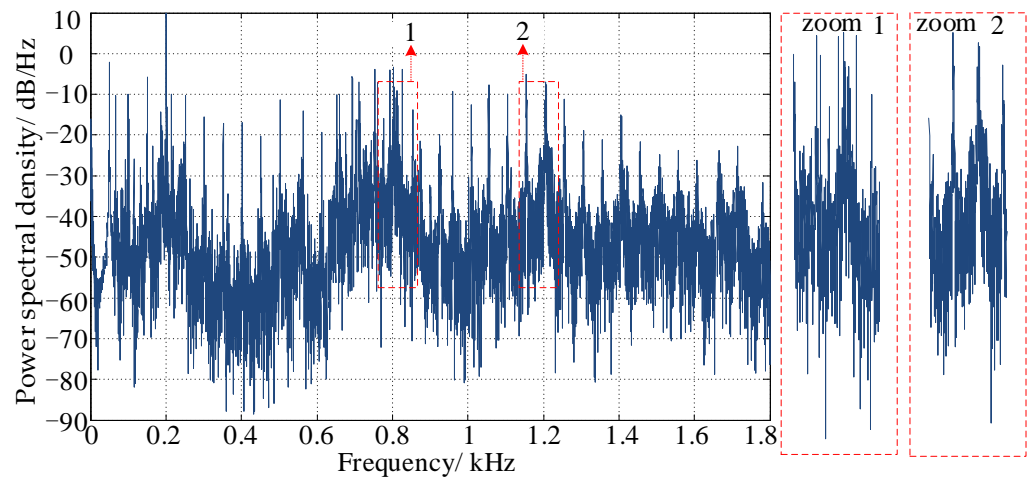


Figure 27. The power spectral density of vibration in IM without compensation.

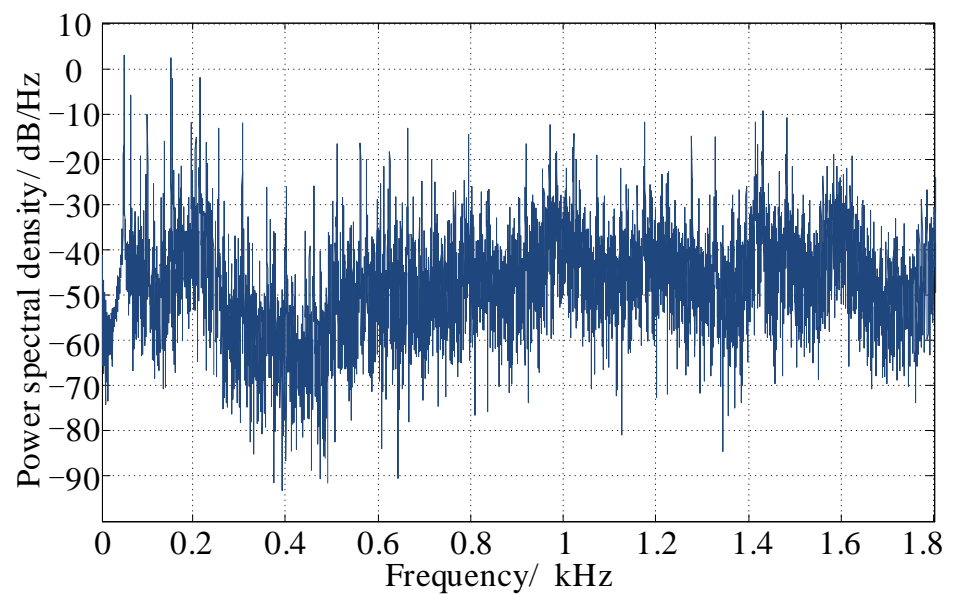


Figure 28. The power spectral density of vibration in IM 6th harmonic controller.

7. Conclusions

The simulation and experimental results prove that the proposed 6th harmonic controller with its parameter design method in d-q axis has good effects on reducing the 5th and 7th harmonic distortion of the stator current, weakening the low-frequency resonance of the motor, and improving the dynamic performance of the motor drive system. Finally, the following conclusions are formed:

- (1) The dead time and the conduction voltage drop of the switching tube and body diode will produce nonlinear errors in the inverter output voltage. The current PI controller based on rotor flux orientation cannot suppress the 5th and 7th harmonic distortion of the stator current caused by the nonlinear voltage;
- (2) Based on current loop stability and the harmonic suppression effect, according to the bode plot and the pole distribution diagram, the proposed 6th harmonic controller can effectively suppress the low-order harmonic distortion of the nonlinear voltage, without generating harmonic distortion of other frequencies, and does not affect the control performance of the current loop;
- (3) Since another resonant controller for the low-speed range is introduced, low-order harmonic suppression at all operating frequencies can be achieved;
- (4) Suppressing the 6th harmonic component of the stator current in d-q axis is an effective means to weaken the low-frequency resonance and vibration of the motor.

Author Contributions: Conceptualization and methodology, P.S.; simulation, Y.L.; validation and experiment, P.S. and T.L.; writing and supervision, L.W. and T.L.; review and editing, P.S.; funding acquisition, H.W. All authors have read and agreed to the published version of the manuscript.

Funding: This work was supported by “the Fundamental Research Funds for the Central Universities”, Southwest Minzu University (Funder, Huazhang Wang; Funding number, 2021101).

Data Availability Statement: Not applicable.

Conflicts of Interest: The authors declare no conflict of interest.

References

1. Du, G.; Zou, Y.; Zhang, X.; Guo, L.; Guo, N. Heuristic Energy Management Strategy of Hybrid Electric Vehicle Based on Deep Reinforcement Learning with Accelerated Gradient Optimization. *IEEE Trans. Transp. Electrification*. **2021**, *7*, 2194–2208. [[CrossRef](#)]
2. Liang, J.; Howey, B.; Bilgin, B.; Emadi, A. Source of Acoustic Noise in a 12/16 External-Rotor Switched Reluctance Motor: Stator Tangential Vibration and Rotor Radial Vibration. *IEEE Open J. Ind. Appl.* **2020**, *1*, 63–73. [[CrossRef](#)]
3. Miao, Y.; Liu, H.; Zhang, W.; Liu, P. Optimal Control Strategy of Storage Inductor Current and Rotor Flux for Current Source Inverter Motor Drive System. *Proc. CSEE* **2019**, *39*, 2757–2767.
4. Song, P.; Liu, Y.; Liu, C. Research on Parameter Design and Control Method for Current Source Inverter-Fed IM Drive Systems. *Machines* **2022**, *10*, 922. [[CrossRef](#)]
5. Jiang, Z.; Ying, D.; Jian, S. Electromagnetic Noise Characteristics of Permanent Magnet Synchronous Motor Applied in Electric Vehicle. *Trans. China Electrotech. Soc.* **2016**, *31*, 53–59.
6. Dong, Z.; Liu, C.; Song, Z.; Liu, S. Suppression of Dual-Harmonic Components for Five-Phase Series-Winding PMSM. *IEEE Trans. Transp. Electrification*. **2022**, *8*, 121–134. [[CrossRef](#)]
7. Lai, Y.-S.; Chang, Y.-T.; Chen, B.-Y. Novel Random-Switching PWM Technique with Constant Sampling Frequency and Constant Inductor Average Current for Digitally Controlled Converter. *IEEE Trans. Ind. Electron.* **2013**, *60*, 3126–3135. [[CrossRef](#)]
8. Peng, H.; Heping, L.; Yiru, M.; You, X.; Guo, Q. Variable Switching Frequency Pulse Width Modulation for Induction Motors based on Current Ripple Peak Value. *Trans. China Electrotech. Soc.* **2020**, *35*, 4373–4383.
9. Liu, P.; Xu, J.; Sun, M.; Yuan, J.; Blaabjerg, F. New Discontinuous Space Vector Modulation Strategies for Impedance-Source Inverter with Superior Thermal and Harmonic Performance. *IEEE Trans. Ind. Electron.* **2022**, *69*, 13079–13089. [[CrossRef](#)]
10. Guo, Q.; Dong, Z.; Liu, H.; You, X. Nonlinear Characteristics Compensation of Inverter for Low-Voltage Delta-Connected Induction Motor. *Energies* **2020**, *13*, 590. [[CrossRef](#)]
11. Liu, P.; Xu, J.; Yang, Y.; Wang, H.; Blaabjerg, F. Impact of Modulation Strategies on the Reliability and Harmonics of Impedance-Source Inverters. *IEEE J. Emerg. Sel. Top. Power Electron.* **2020**, *8*, 3968–3981. [[CrossRef](#)]
12. Zhang, Z.; Xu, L. Dead-Time Compensation of Inverters Considering Snubber and Parasitic Capacitance. *IEEE Trans. Power Electron.* **2014**, *29*, 3179–3187. [[CrossRef](#)]
13. Liu, H.; Liu, Q.; Zhang, W.; Miao, Y.; Liu, P. Random PWM Technique for Acoustic Noise and Vibration Reduction in Induction Motors used by Electric Vehicles. *Trans. China Electrotech. Soc.* **2019**, *34*, 1488–1495.

14. Kobayashi, T.; Tajima, F.; Ito, M.; Shibukawa, S. Effects of Slot Combination on Acoustic Noise from Induction Motors. *IEEE Trans. Magn.* **1997**, *33*, 2101–2104. [[CrossRef](#)]
15. Gao, X.; Su, D. Suppression of a Certain Vehicle Electrical Field and Magnetic Field Radiation Resonance Point. *IEEE Trans. Veh. Technol.* **2018**, *67*, 226–234. [[CrossRef](#)]
16. Wu, Z.; Ding, K.; Yang, Z.; He, G. Analytical Prediction and Minimization of Deadtime-Related Harmonics in Permanent Magnet Synchronous Motor. *IEEE Trans. Ind. Electron.* **2021**, *68*, 7736–7746. [[CrossRef](#)]
17. Liu, H.; Lu, Y.; Wang, H.; Miao, Y. Dead-time Compensation Modulation Strategy of Subsection Integrated in Voltage Source Inverter. *Electr. Mach. Control* **2018**, *22*, 25–32.
18. Miao, Y.; Liu, H.; Wang, H.; Lu, Y. Average Current Feedforward Compensation Strategy of Overlap-Time Effect for Current Source Inverter. *Proc. CSEE* **2018**, *38*, 4183–4193.
19. Liao, Y.; Zhen, S.; Liu, R.; Yao, J. Torque Ripple Suppression of Permanent Magnet Synchronous Motor by the Harmonic Injection. *Proc. CSEE* **2011**, *21*, 119–127.
20. Yang, Y.; Zhou, K.; Wang, H.; Blaabjerg, F.; Wang, D.; Zhang, B. Frequency Adaptive Selective Harmonic Control for Grid-Connected Inverters. *IEEE Trans. Power Electron.* **2015**, *30*, 3912–3924. [[CrossRef](#)]
21. da Silveira, D.B.; Farias, J.V.M.; Pereira, H.A.; Luiz, A.-S.A.; Stopa, M.M.; Cupertino, A.F. Mitigation of torque oscillations caused by dc injection-based resistance estimation through resonant controllers. In Proceedings of the 2021 Brazilian Power Electronics Conference (COBEP), João Pessoa, Brazil, 7–10 November 2021; pp. 1–6.